CHEMISTRY

Uneven phosphoric acid interfaces with enhanced electrochemical performance for high-temperature polymer electrolyte fuel cells

Zinan Zhang[1,2,3]†, Zhangxun Xia[1,3]†, Jicai Huang[1,3], Fenning Jing[1,3], Xiaoming Zhang[1,3], Huanqiao Li[1,3], Suli Wang[1,3]*, Gongquan Sun[1,3]*

Ultrahigh mass transport resistance and excessive coverage of the active sites introduced by phosphoric acid (PA) are among the major obstacles that limit the performance of high-temperature polymer fuel cells, especially compared to their low-temperature counterparts. Here, an alternative strategy of electrode design with fibrous networks is developed to optimize the redistribution of acid within the electrode. Via structural tailoring with varied electrospinning parameters, uneven migration of PA with dispersed droplets is observed, subverting the immersion model of conventional porous electrode. Combining with experimental and calculation results, the microscaled uneven PA interfaces could not only provide extra diffusion pathways for oxygen but also minimize the thickness of PA layers. This electrode architecture demonstrates enhanced electrochemical performance of oxygen reduction within the PA phase, resulting in a 28% enhancement of the maximum power density for the optimally designed electrode as cathode compared to that of a conventional one.

INTRODUCTION

Manufacturing, storage, and delivering highly purified hydrogen are major challenges for the commercialization of polymer electrolyte fuel cells (PEFCs) (*1*). On-site hydrogen production from liquid fuel (methanol, ethanol, diesel, gasoline, etc.) reforming coupled with high-temperature (>150°C) polymer electrolyte fuel cells (HT-PEFCs) based on phosphoric acid (PA)–doped polybenzimidazole (PBI) membrane is recognized as a promising solution (*1*–*3*), especially for combined heat and power (CHP) systems, heavy-duty vehicles, and low-emission marine powers (*4*, *5*). However, insufficient performance with relatively inferior specific power (one-third to one-half of PEFCs) limits the widespread application of HT-PEFCs (*6*, *7*).

Different from the LT-PEFCs with perfluorosulfonic acid (PFSA) ionomer as proton carriers in electrodes, liquid PA is adopted to form a proton-conductive phase and electrochemical interfaces within the porous electrodes of HT-PEFCs (*8*), leading to ultrahigh mass transport resistance and catalyst poisoning (*9*, *10*). PA adsorption on the platinum surface blocks the active sites for oxygen reduction reaction at the cathode, while oxygen solubility and diffusion coefficient in PA are lower than that in water or PFSA electrolyte by orders of magnitude (*11*, *12*). In addition, because of its fluid nature, PA leaching will reduce performance under lifetime test circumstances. To conquer these defects in material and structural aspects, milestones have been achieved in recent decades. The adoption of PBI as polymer electrolyte for HT-PEFCs partially immobilizes PA with the imidazole groups at a relatively high temperature (*8*). Most recently, polymer based on quaternary ammonium salt with stronger PA binding energy, associated with the organic PA polymer as an ionomer in the porous electrode (*13*, *14*), has been presented to further reduce and redistribute PA with enhanced cell performance and durability (*15*). Hence, the chemical status and distribution behavior of PA within the electrode should be crucial for the engineering development of HT-PEFCs. The fluidity of PA leads to an unstable three-phase boundary structure, while PA accumulates in the cracks of the catalytic layer to easily form closed-off pores, leading to considerable transport resistance of reactant gasses (*16*). As smaller cracks require higher capillary pressure to be flooded (*17*), Büchi and coauthors (*18*) fabricated catalyst layers with 70% reduced crack size less than 20 μm and found that it was unable to penetrate the entire catalyst layer even at an acid pressure of PA of 84 mbar. Furthermore, blocking the crack connectivity to reduce PA accessibility in the catalyst layer could also mitigate PA penetration from catalyst layer (CL) to microporous layer (MPL) (*19*). To balance the proportion of cracks for PA penetration and gas transport, the binders have a key role to determine that the catalyst layer is H_3PO_4-uptake type or waterproof type (*20*, *21*). H_3PO_4-uptake binders, such as PBI polymer, accelerated PA distribution in CL but easily lead to acid flooding (*22*, *23*). Alternative waterproof binders such as polyvinylidene fluoride or polytetrafluoroethylene (PTFE) could enhance gas transport due to restraining the PA coverage on the Pt catalyst (*22*, *24*, *25*).

Although reduced penetration of PA toward the porous electrode could lead to a loss of electrochemical surface area (ECSA), antiwetting of PA is still favored to result in better performance. The superhydrophobic property of materials derived from surface engineering in micro/nanoscale is recognized as a promising strategy to adjust the wetting behavior and distribution of liquid (*26*, *27*). With the reduced surface energy, a fibrous architecture proposes great hydrophobic performance to efficiently transport and repel water for multiple applications (*28*, *29*). In LT-PEFCs, electrodes with fibrous structures provide much optimized water management under real working circumstances for their rapid draining of the

[1]Division of Fuel Cell and Battery, Dalian National Laboratory for Clean Energy, Dalian Institute of Chemical Physics, Chinese Academy of Sciences, Dalian 116023, China. [2]University of Chinese Academy of Sciences, Beijing 100049, China. [3]Key Laboratory of Fuel Cell and Hybrid Power Sources, Dalian Institute of Chemical Physics, Chinese Academy of Sciences, Dalian 116023, China.
†These authors contributed equally to this work.
*Corresponding author. Email: suliwang@dicp.ac.cn (S.W.); gqsun@dicp.ac.cn (G.S.)

extra water generated from the cathode reaction (*30*, *31*). However, viewpoints of the fluidic PA well organized and rearranged within the porous electrode to accelerate the mass transport processes in HT-PEFCs have not been considered yet.

Here, focusing on the reduction of oxygen mass transport resistance for HT-PEFCs, uneven PA interfacial layers with dispersed droplets are first presented by construction of the fibrous electrode architecture. Ascribing to the ultrahydrophobic nature of the nanofiber networks, PA agglomeration occurs as forms of noninfiltration droplets in the size of micrometer scale, subverting the traditional immersion model of PA under working circumstances. Experimental results of the limiting current methods, combined with theoretical studies, demonstrate a considerable decrease in mass transport resistance in the PA phases and enhanced electrochemical active areas with such an uneven interfacial structure, leading to notable performance enhancement compared to that of the conventional electrode.

RESULTS

Morphological and physical characterization

The fibrous networks with hierarchically porous structures could be fabricated via a facile electrospinning method, as illustrated in Fig. 1A. Briefly, catalyst nanoparticles (PtCo/C) were dispersed in deionized water mixed with PTFE as a waterproof agent and polyvinyl alcohol (PVA) as an electrospinning carrier polymer (*32*). The electrospun fibrous networks could be directly fabricated on the substrate of an aluminum foil. The as-prepared composite fibers were then sintered to remove the PVA with the porous structure remaining, consisting of catalyst particles and PTFE (denoted as ESFE) (*33*). The composition information of the samples and materials is evidenced in their x-ray diffraction (XRD) and thermal gravimetric (TG) test results, as shown in Fig. 1 (B and C, respectively). XRD patterns (Fig. 1B and fig. S1) confirm the removal of PVA as the peaks of PVA are absent in the samples of ESFE, which are observed in the ESFE precursor (ESFE-pre). Meanwhile, the peaks of PTFE in the XRD patterns appear in both ESFE-pre and ESFE (except the samples without PTFE), indicating that PTFE is stable under this sintering process. TG analyses further validate the composition change of the samples with quantified information, as shown in Fig. 1C and fig. S2. The decomposition temperature of PVA is around 230° to 260°C, whereas such temperature is over 500°C for PTFE. Hence, the pyrolysis temperature of the ESFE samples is set as 320°C to guarantee the removal of PVA and the remaining PTFE, as evidenced above. The quantified content of different materials could have resulted in the weight change of the TG curves, as listed in table S1.

The morphological details of the fibrous electrode samples could be found in the scanning electron microscopy (SEM) images, as shown in Fig. 1 (D to F) and figs. S3 and S4. Before the pyrolysis process, the ESFE-pre samples present obvious fibrous networks with combined knotty and smooth fibers. The average diameter of the fibers is about 185 nm for samples with varied PTFE content. After the pyrolysis treatment at 320°C with nitrogen, much uniform fibrous networks with a rough surface are demonstrated in a hierarchical porous architecture with the exposure of the catalyst particles. The average diameter is slightly increased to 210 nm for different samples with varied PTFE content by the PVA transformed into carbon. A cross-sectional view of the ESFE samples (fig. S4, E to H) demonstrates a freestanding structure as the catalyst layers with average thickness of 48 to 53 μm (table S2), slightly larger than the conventional catalyst layers attached to the gas diffusion layers (fig. S4, A to D). Brunauer-Emmett-Teller characterization of the porous structure for the different samples further indicates that an increased proportion of micro/mesopores is observed in ESFE samples, compared to conventional ones, as

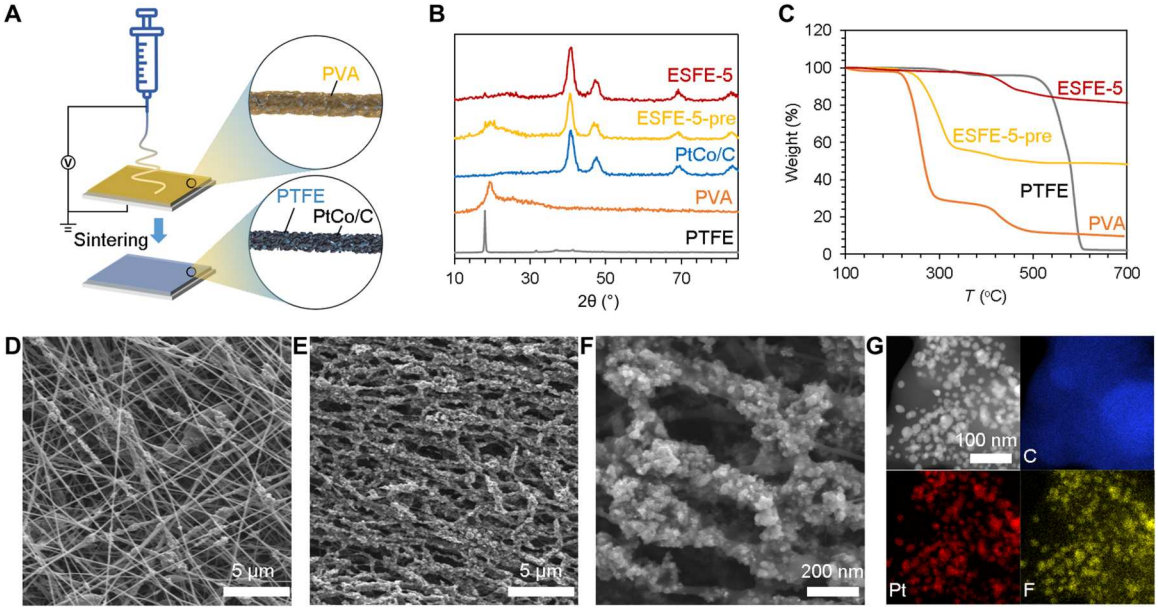

Fig. 1. The preparation process, morphology, and composition characterizations of ESFE. (**A**) Schematic of the electrode fabrication processes via electrospinning method. (**B** and **C**) XRD patterns (B) and TG results under Ar atmosphere (C) compared with PVA, PTFE, and PtCo/C catalyst. (**D** to **F**) SEM images of the electrospun sample before (D) and after (E and F) heat treatment. (**G**) Scanning transmission electron microscopy image and element mapping.

shown in fig. S5 and table S2. Further characterization of the distribution of the material within the fibers is conducted via elemental mapping, as shown in Fig. 1G. The distributions of Pt and F are observed to be highly consistent, suggesting uniform combination of the catalyst and PTFE via the fabrication processes of electrospinning and pyrolysis. This unique architecture of the electrode could present benefits for mass transport and PA management under dynamic conditions.

In situ characterization of the PA distribution

In the real working circumstance of HT-PEFCs, PA acts as proton carriers covering the catalyst particles to form electrochemical interfaces. The transport behavior and distribution of PA crucially relate to the morphology and chemical properties of the porous electrodes. To clarify the PA distribution within the different electrode samples, a simulated environment is set up within the chamber of an environmental scanning electron microscopy (ESEM) based on a previous study (*34*). Briefly, PA is first introduced to the as-prepared electrode samples via hot-pressing with PA-doped PBI membrane as membrane electrode assemblies (MEAs) and activation in real working circumstances with 200 mA cm^{-2}. Then, the electrode samples are disassembled from the MEAs, and the test environment (temperature and pressure) is adjusted to simulate the real working conditions according to the saturated vapor pressure curve of the PA solutions, as shown in fig. S6 (*35*). Hence, the distribution change of PA within the porous electrodes under open circuit voltage and lower current density (dry circumstance with less water generated) to higher load (humidified circumstance with a great amount of water generated) could be simulated with the change of test temperature. Detailed experiments could be found in Materials and Methods. Figure 2A demonstrates the PA immersion of the conventional porous electrode with the humidifying process. The volume expansion of the liquid phase brought by the moisture of PA leads to even filling of the pores, ascribing to the hydrophilic nature toward the PA solution (insert image of Fig. 2A). This dynamic process could be observed in movie S1. It is worth noting that the liquid PA solution could flood the whole surface in the case of a hydrophilic circumstance such as an electrode without PTFE (CE-0) or PA-doped PBI membranes, as shown in fig. S7. As a result, it could indicate that the PA flooding phenomenon would cover most of the pores for gas transport and the surface of the catalyst under the working conditions of HT-PEFCs, as schemed in Fig. 2B.

The electrode sample with fibrous structure presents an entirely different phenomenon of PA immersion, as shown in Fig. 2C and movie S2. First, the contact angle of PA solution on the surface of the fibrous electrode is obviously greater than that of the conventional ones, as shown in the insert photo of Fig. 2C. With the humidifying process under the simulated environment of the ESEM test, the forming of PA solution droplets occurs instead of the immersion process observed in the conventional sample. The hydrophobic droplets accommodate the volume expansion of the moisture of PA, and the unoccupied pores and catalyst surfaces could be retained for mass transport and reactions, as illustrated in Fig. 2D. The diameter and volume fraction distribution of the droplets are diagramed in Fig. 2F based on the ESEM images under a full humidified condition. The average diameter of the PA solution droplet is 18 μm, whereas the droplets with larger size (25 to 35 μm) take most of the liquid phase volume, suggesting that the surface of the catalyst particles is covered by much thinner PA layers.

The acid-proof nature of the fibrous electrode could be introduced by the unique network structure of the hybrid materials. The wetting behavior and the contact angle of PA solution on the samples with different PTFE content for the conventional and fibrous electrodes are shown in Fig. 2G and fig. S8A. With the increase in PTFE content, contact angles increase for the two series of the samples, whereas the contact angles for the fibrous electrodes are much greater than that of the conventional one. It is worth noting that a considerable hydrophobic property toward both PA and water (fig. S8B) is observed in the ESFE sample without PTFE, indicating that such enhanced acid-proof nature could be brought about by the nanofibrous network architecture. Plenty of studies have elucidated such phenomena on the material and structural aspects (*36*). The Cassie-Baxter model rationally demonstrates this wetting behavior in which the droplet is energetically favorable to bridge across the tops of the nanowires to form air gaps between the droplet and the flat surface (*37*).

Single-cell performance of the fibrous electrodes

As the performance of HT-PEFCs crucially relates to the distribution of PA within the electrode, polarization curves of the single cells equipped with the fibrous electrodes with different PTFE content as cathodes are tested, as shown in Fig. 3. For the case of cathodes fed with oxygen, the mass transport resistance of cathodes is minimum, leading to close polarization performance with different PTFE content for both fibrous (Fig. 3A) and conventional samples (fig. S9A). In addition, the samples with fibrous electrodes present much greater performance in oxygen compared to the conventional electrodes with the same PTFE content, suggesting high catalyst utilization with the tailored electrode architecture. When cathodes are fed with air, the mass transport resistance of oxygen is non-negligible, leading to great performance loss, as shown in Fig. 3B. The sample without PTFE (ESFE-0) demonstrates markedly reduced polarization performance, whereas other samples present similar values. Considering that ESFE-0 shows the lowest contact angle toward PA, the enhanced mass transport resistance induced by PA flooding should be the major reason for such performance loss. Furthermore, the highest polarization performance is demonstrated in the sample of ESFE-5, despite the acid-proof property for this sample being not the best, suggesting that the increased PTFE might cover the active sites of the catalyst and then reduce the activation performance of the single cells. Compared to the conventional electrode, the peak power density of the single cell with ESFE-5 is 414 mW cm^{-2}, which is 28% higher than that of the conventional one, as shown in Fig. 3C. The peak power density of the series samples with fibrous electrodes is superior compared to the series of the conventional ones, as shown in Fig. 3D, indicating that the superiority in polarization performance could be provided by the unique fibrous electrode architecture. This performance enhancement is further demonstrated in electrochemical impedance spectroscopy (EIS) and cyclic voltammetry (CV) results, as shown in figs. S10 and S11, respectively. Compared to the conventional electrode, the charge transfer resistance (R_{ct}) fitted from the EIS data markedly reduced (table S3), indicating that the electrochemical dynamic processes could be accelerated as the reduced coverage and poisoning of PA. The construction of the unique porous architecture with uneven PA distribution also provides a much larger

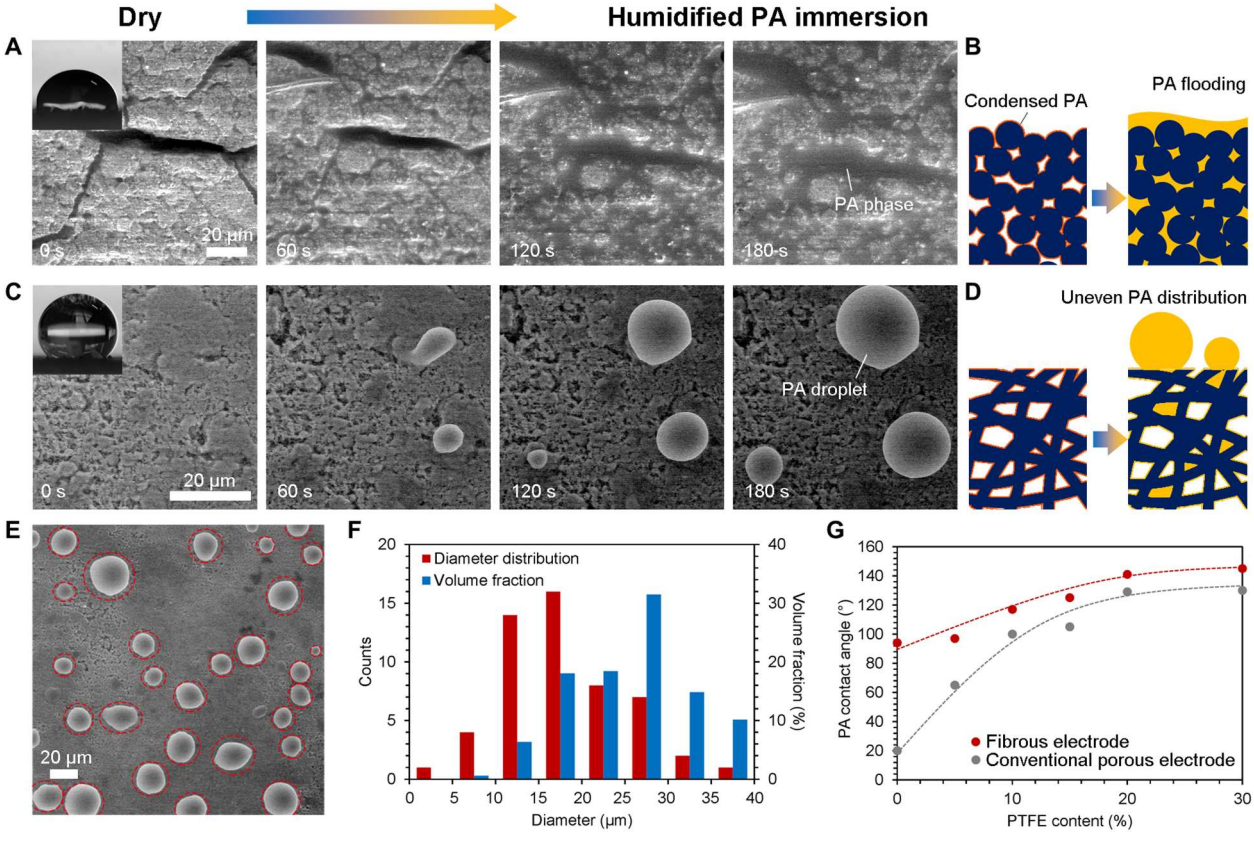

Fig. 2. PA distribution behavior within different electrode architecture. (**A** and **C**) ESEM images for the conventional (A) and the fibrous (C) electrode with PA under varied humidification. (**B** and **D**) PA distribution models for the corresponding electrode samples. (**E** and **F**) Statistic histograms (F) of the PA droplets obtained from the ESEM images (E) under full humidification. (**G**) Contact angles of PA solution tested on the different samples.

ECSA for electrochemical reactions, as shown in the data calculated from the CV curves. Furthermore, the durability performance of the ESFE sample under working circumstance is further analyzed with a lifetime test under a constant current density of 200 mA cm^{-2}, as shown in Fig. 3E. After a 300-hour test, the single cell equipped with ESFE-5 demonstrates remarkable stability without observable voltage loss. The single-cell performance of this fibrous electrode also achieves a leading level among the research reported recently in HT-PEFCs, as shown in table S4, bringing great application potential, especially for heavy-duty vehicles and stationary CHP.

Oxygen mass transport analyses of the uneven PA interfaces

The advantages of the fibrous electrodes in mass transport issues are further studied with both experimental and theoretical analyses, as shown in Fig. 4. First, to calculate the mass transport resistance within the electrodes, the method based on limiting current density is adopted as described in Materials and Methods (*38*). In the test protocol, cathodes fed with 1% oxygen ensure that the cell voltage is controlled by mass transport at a high current density. The values of the current at 0.2 V are recorded as the limiting current density because, at low voltage (<0.15 V), hydrogen evolution current could be more obvious (*39*). Figure 4A and fig. S12 demonstrate the polarization curves recorded in the limiting current density tests with different inert diluent gas for the electrode samples. With the limiting current density, resistance for the total oxygen transport (R_{total}), molecular diffusion in the gas phase (R_M), and transport within the PA phase (R_{PA}) could be calculated on the basis of the equations provided in Materials and Methods. The limiting current density for the ESFE samples is observed to be higher than that of the conventional one with the same PTFE content, indicating much reduced mass transport resistance for oxygen. The calculated R_M and R_{PA} values are demonstrated as shown in the histograms of Fig. 4B and table S5. R_M for the fibrous electrodes is observed to be much smaller than that of the conventional electrode with any PTFE content in both He and nitrogen balance gas. R_M is determined by the effective molecular diffusion distance (h_M^{eff}) and oxygen diffusion coefficient (D_{M,O_2}), and h_M^{eff} is related to the structure of the electrode, as the following equation

$$R_M = \frac{h_M^{eff}}{D_{M,O_2}} \quad (1)$$

The network structure of the fibrous electrodes with a great number of open pores could facilitate gas accession compared to that of the conventional porous electrodes and provides a much smaller diffusion distance within the electrode (*40*). The ratio of R_M in R_{total} is about 30% for nitrogen as the balance gas, higher than the situation with He (ca. 10%), as D_{M,O_2} in nitrogen is much higher than that in He. However, in any case of the test results, R_M contributes a small part to R_{total}, suggesting that the

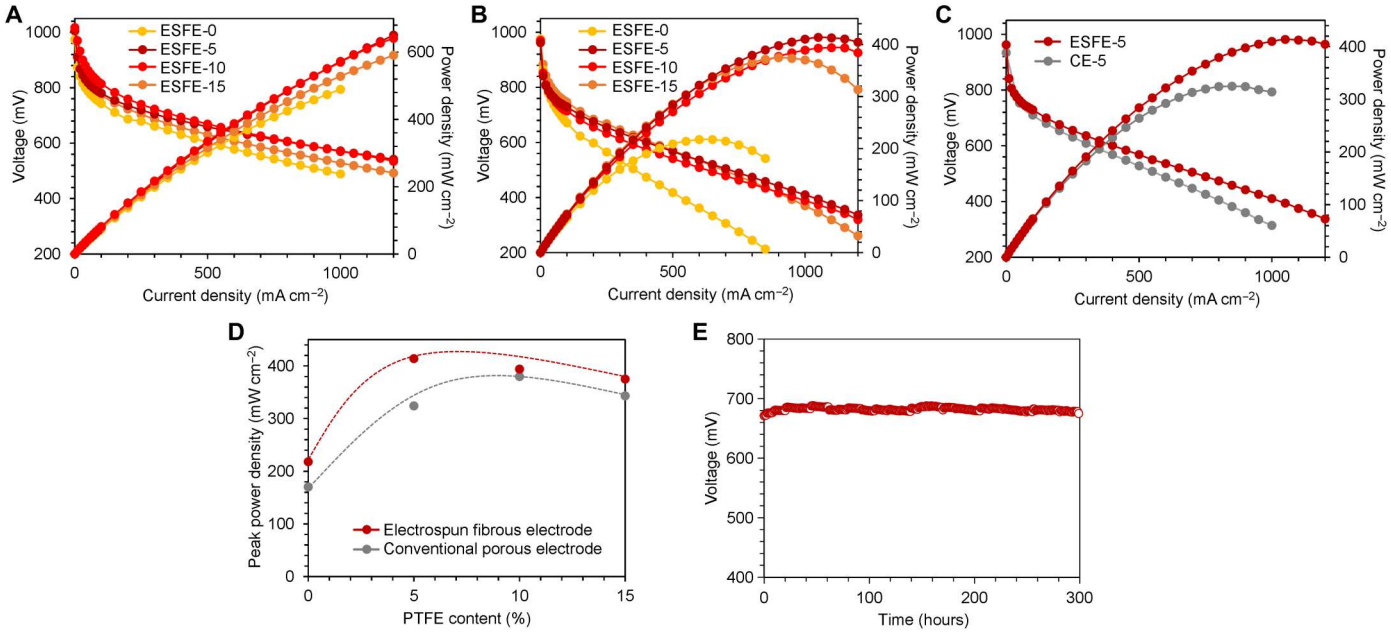

Fig. 3. Single-cell performance of ESFE and CE. (**A** and **B**) ESFE polarization curves and power density fed with (A) H_2/O_2 (A/C) and (B) H_2/air. (**C**) Polarization curves and power density of ESFE-5 versus CE-5 under H_2/air. (**D**) The peak power density functioned with PTFE content. (**E**) Lifetime test of the single cell with ESFE at a constant current density of 200 mA cm^{-2}.

resistance in PA is the major factor. The lowest value of R_{PA} is observed with 81.48 s m^{-1} in the sample of ESFE-5, which is 32% lower than that of the conventional one, confirming the deduction that the uneven PA distribution could improve mass transport within the PA phase. It is worth noting that, compared to the interfacial resistance obtained in the LT-PEFCs with PFSA ionomer as proton carriers, R_{PA} in HT-PEFCs is much higher, as shown in table S6. By summarizing the interfacial resistance and power density for LT-PEFCs and HT-PEFCs, it could be further claimed that the extra mass transport resistance within the PA layers of the electrodes acts as the major factor, limiting the performance of HT-PEFCs, as shown in fig. S13.

To further clarify the oxygen transport with the differently distributed PA, calculation is conducted on the basis of the morphological characterization results, as shown in Fig. 4 (C and D). Here, the geometric model of the PA interfaces is simplified because of the droplet size of PA being up to tens of micrometers, multiple orders of magnitude larger than the nanosized pores of the catalyst layers. Hence, the effect of porous structure on the PA distribution is simply described by the contact angle of PA on a flat surface of electrodes. As described in Fig. 4D, contact angle is set as the variable, and the transport distance of oxygen through the PA layer is varied by assuming that the total volume of PA is constant. Relative R_{PA} could be calculated with the change of the contact angle, as shown in Fig. 4C. Compared to the tendency of the tested values of R_{PA}, experimental data fit closely with the theoretical curve, suggesting that the elucidation of the uneven PA distribution is reasonable. On the basis of this model of PA layers, computational fluid dynamics (CFD) is also adopted to analyze the oxygen diffusion within the PA phase, as shown in Fig. 4D and fig. S14. The simulation is conducted by the volume of fluid model with unsteady state, which is widely used to study the droplet behavior for its accurate interface tracking technique. Combining the species transfer model in the CFD software, the droplet behavior and mass transfer of oxygen can be predicted. The flat layer thickness of the PA phase for oxygen diffusion reduces with the increase in the contact angle of the PA droplets, leading to much more efficient transport processes of oxygen from the gas phase to the active surface of the catalyst. Despite the transport resistance in the PA droplet spots being increased, the uncovered surface could provide larger areas with accelerated mass transport.

DISCUSSION

By understanding the performance limitation of HT-PEFCs derived from the interfacial mass transport resistance within PA layers, an electrode-designing strategy to regulate the distribution of PA with uneven status is proposed in this work. On the basis of the PA wetting behavior toward porous electrode, a fibrous nanoarchitecture constructed by a catalyst and a hydrophobic component is achieved via electrospinning processes. Subverting the PA infiltration model in the conventional porous electrode, micrometer-scale PA droplets are formed and observed under the simulated working circumstance. This uneven distribution of PA provides reduced thickness and coverage of the PA layers on the catalyst, leading to a 32% decrease in oxygen interfacial transport resistance and much enhanced ECSA compared to that of the conventional one. As a result, the peak power density of the fibrous electrode reaches 414 mW cm^{-2}, 28% greater than that of the conventional porous electrode, demonstrating great application potential of HT-PEFCs. Further theoretical analyses based on the geometric model of the PA distribution confirm such enhancement in mass transport and shed light on the development of advanced MEAs for HT-PEFCs with sufficient values of application.

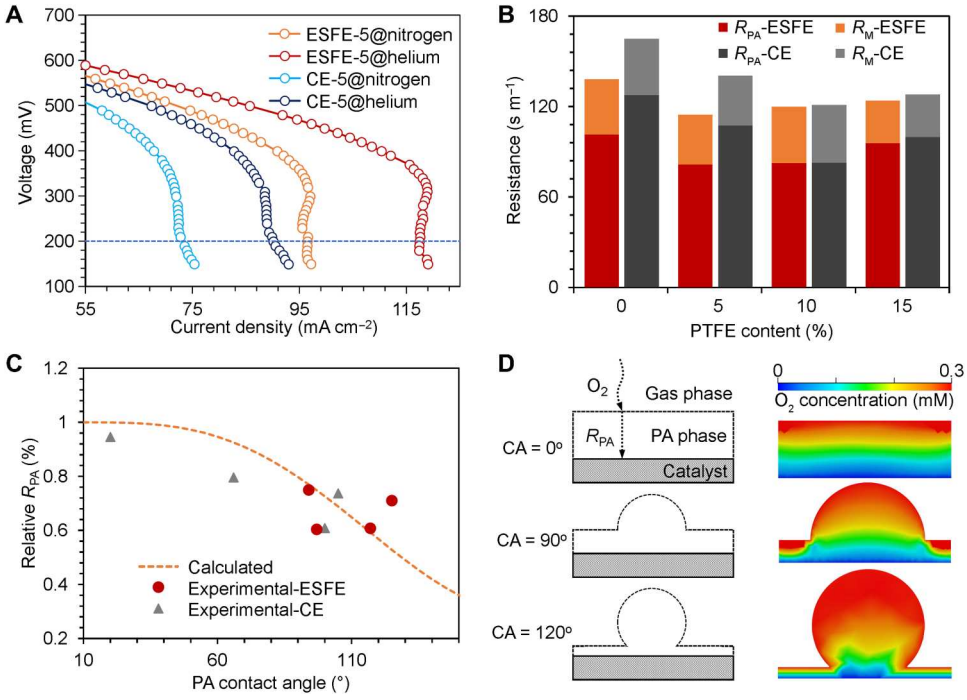

Fig. 4. Study on the mass transport within different structures. (**A**) The limit current tests in 1% O_2 with balance gas of nitrogen or He for different electrode samples. (**B**) Histogram of the calculated mass transport resistance. (**C**) Relative R_{PA} obtained from the theoretical calculation and experiments. (**D**) Geometric models and oxygen diffusion simulation of the PA layers with different contact angles.

MATERIALS AND METHODS

Chemicals and materials

Phase-separated polymer solutions of PTFE [60 weight % (wt %)] were obtained from Shanghai 3F New Materials Technology, PVA (PVA1750) was acquired from Tianjin Guang Fu, 5% Nafion ionomer was purchased from DuPont, Tanaka Kikinzoku Kogyo PtCo/C catalysts (47.1 wt % Pt and 4.5 wt % Co) were used for all cathode electrode, and Johnson Matthey Chemicals Pt/C catalysts (60 wt % Pt) were used for all anode electrodes.

Fabrication of nanofibrous catalyst layers

A PtCo/C catalyst was used as the active component, PVA was the electrospinning carrier polymer, and PTFE was the hydrophobic component to prepare the electrospinning inks. Inks were made in a deionized water solvent. The solid content of inks was about 7 wt %, the carrier polymer content was no more than 50 wt % of the solid mass, the mass ratio of PTFE:PtCo/C catalyst was added in proportion (0, 5, 10, 15, 20, and 30 wt %), and the mass ratio of Nafion:PtCo/C catalyst was fixed at 13 wt %. Electrospinning inks were prepared as follows: Catalyst, PTFE, 5 wt % Nafion solution, and water were mixed, and then the mixture was sonicated for 30 min. Next, a 5 wt % PVA aqueous solution was added, and the mixture was mechanically stirred while sonicating in cold water for 30 min. Last, the ink was mixed for 4 hours using a mechanical stirrer at room temperature.

Electrospinning ink was filled into a 5-ml syringe with a 21-gauge metal needle, which relates to a DC voltage supply. The syringe was placed into a syringe pump with a solution flow rate of 0.3 ml/hour. Aluminum foil was coated on a grounded metal roller collector. Nanofiber was electrospun with a needle-to-collector distance of 10 cm, relative humidity of 20 to 30%, and a voltage of 16 to 20 kV. Nanofiber mat was torn to square and layered on top of each other to create a catalyst layer, with a Pt loading of 1.0 mg cm^{-2} by weighting. All nanofiber catalyst layers were heated at 320°C for 300 min under a nitrogen atmosphere.

Fabrication of conventional electrodes

Cathode gas diffusion electrode (GDE) was prepared as follows: We (i) stirred PTFE, PtCo/C catalyst, and water mixture for 2 hours at 90°C; (ii) vacuum-filtered the mixture; (iii) added 50% ethanol to the filter cake and sonicated for 30 min; (iv) sprayed catalyst ink on commercial gas diffusion layers (GDLs) (TGP-H-060, Toray Industries); and (v) heated the GDE for 30 min at 300°C under nitrogen atmosphere. The Pt loading was about 1.0 mg cm^{-2}. A series of conventional cathode electrodes with different PTFE mass content (0, 5, 10, 15, 20, and 30 wt %) was prepared following this method. All the anode GDEs were fabricated with Pt/C catalysts with a Pt loading of 0.5 mg cm^{-2} and PTFE content of 10% following the same procedures.

Fabrication of MEA

The MEA adopted a sandwich structure in which the anode GDE, PA-PBI membrane (Fumapem AMcl), and cathode GDE (nanofiber catalyst layer and GDL) were placed in sequence. The active area of each MEA is 2 cm × 2 cm.

Single-cell performance test and oxygen mass transport resistance measurement

The single cell was assembled as described in (*41*). Conventional and electrospun MEAs were compressed by a ratio of 20 to 30%.

Cathode gas was humidified at 30°C. The electrochemical tests were based on a homemade fuel cell test system, and the operating conditions are shown in Table 1.

The method of measuring mass transport resistance and separating the oxygen transport resistance is based on the study on the LT-PEFCs (see the Supplementary Materials) and a previous study (*42*). The oxygen concentration on the catalyst surface is zero when the oxygen diffusion rate reaches the limit value. Therefore, the oxygen transport rate is equal to its consumption rate, and the total oxygen resistance (R_{total}) from the channel to the catalyst surface is represented as follows

$$N_{O_2}^{trans} = \frac{C_{O_2}^{FF} - 0}{R_{total}} = N_{O_2}^{react} = \frac{i_{lim}}{4F} \quad (2)$$

$$R_{total} = \frac{4FC_{O_2}^{FF}}{i_{lim}} \quad (3)$$

Here, N is the molar flux rate per unit area (moles per square meter per second), F is the Faraday constant (96,485 C mol^{-1}), $C_{O_2}^{FF}$ is the oxygen concentration in flow field (moles per cubic meter), and i_{lim} is the limiting current density (milliamperes per square centimeter). To confirm that i_{lim} is completely controlled by the oxygen mass transport polarization, 1% O_2 is used in this experiment.

R_{total} consists of the following resistance in series

$$R_{total} = R_M + R_K + R_{PA} = R_M + R_{PA} \quad (4)$$

Here, R_M is the molecular diffusion resistance, R_K is the Knudsen diffusion resistance, and R_{PA} is the PA phase diffusion resistance.

With the definition of diffusion resistance, the transport resistance in the gas phase can be expressed as

$$R_{A,B}^{M} = \frac{L}{D_{A,B}} \quad (5)$$

The pressure-dependent part can be obtained using the Fuller-Schettler-Giddings equation (*43*, *44*), which gives the molecular diffusion coefficient ($D_{A,B}$) for a binary gas mixture

$$D_{A,B} = \frac{0.001T^{1.75}}{P\left(v_A^{1/3} + v_B^{1/3}\right)^2}\sqrt{\frac{1}{M_A} + \frac{1}{M_B}} \quad (6)$$

Here, L is the diffusion distance, P is the gas pressure, T is the temperature in kelvin, v_A and v_B are the diffusion volumes of A and B gas, and M_A and M_B are the molar masses. However, humidification and oxygen reduction reaction will introduce water vapor. Oxygen concentration is less than 1% in the limiting current test, simplifying the ternary gas mixtures' molecular diffusion coefficient as

$$\frac{1}{D_{mix}} = \frac{x_B}{D_{A,B}} + \frac{x_C}{D_{A,C}} \quad (7)$$

where the Knudsen diffusion coefficient is expressed as

$$D_k = \frac{d}{3}\sqrt{\frac{8RT}{\pi M_A}} \quad (8)$$

Here, d is the diameter of the pore, and R is the universal gas constant. The contribution of R_M and R_K is mainly dependent on the pore size. It is worth noting that R_K is difficult to be directly calculated because it is hard to find an effective sensitive parameter to conduct the variable separation approach (*45*, *46*). Plenty of literature focused on mass transport issues for fuel cells neglected this factor (or did not separate R_K) to simplify the calculation processes (*38*, *47*). On the other hand, different from the electrodes of LT-PEFCs with solid ionomers as proton carrier, liquid PA could fill the micro/mesopores within the electrodes for HT-PEFCs, leading to a minimized proportion of R_K out of the total resistance, because the diffusion within the PA phase is demonstrated by R_{PA} in this work. Therefore, R_{total} can be simplified as the sum of R_M and R_{PA} (Eq. 4).

According to R_M that can be separated by changing the balance gas and R_{PA} being independent of the balance gas, the R_M of different balance gases with 1% O_2 can be calculated using the following equations

$$R_{PA} = R_{O_2-N_2}^{total} - R_{O_2-N_2}^{M} = R_{O_2-He}^{total} - R_{O_2-He}^{M} \quad (9)$$

$$\frac{R_{O_2-N_2}^{M}}{R_{O_2-He}^{M}} = \frac{D_{O_2-He}^{M}}{D_{O_2-N_2}^{M}} \quad (10)$$

Table 1. The electrochemical test conditions for MEAs. OCV, open circuit voltage.

Operation	T_{cell}	Anode flow	Cathode flow	Test program
Activation	160°C	100 ml min^{-1}, H_2	200 ml min^{-1}, air	200 mA cm^{-2}, 150 hours
V-I test	160°C	100 ml min^{-1}, H_2	200 ml min^{-1}, air	OCV → 0.2 V, 90 s for each point
I_{lim} test	160°C	100 ml min^{-1}, H_2	(1%O_2@N_2/He)	OCV → 0.11 V, ΔI = 1 mA/20 s

Physical characterizations

The morphology of the nanofiber catalyst layer was analyzed by SEM (JSM-7800 F and IT300 LA, JEOL). The PA contact angle was measured by a drop shape analyzer (JC2000C1); the test had been operated at 25°C with a 10-μl droplet. XRD was performed using a Rigaku D/Max-2500 diffractometer. Thermogravimetric analysis curves were tested on SDTQ600 with a heat rate of 10°C min^{-1} under Ar or air flow of 100 ml min^{-1}. PA-containing samples were studied by ESEM (Quanta 650FEG, FEI) with a vapor pressure of H_2O of 500 Pa. To ensure that the amount of PA in the electrode is consistent, the PA-containing electrode was torn from an activated completed MEA and then cut into a disk with a diameter of 5 mm. During the test, two heating and cooling processes were carried out at 15° to 50°C. Videos and photos of the heating and cooling processes were recorded.

Supplementary Materials

This PDF file includes:

Notes S1 and S2
Figs. S1 to S14
Tables S1 to S7

Other Supplementary Material for this manuscript includes the following:
Movies S1 and S2

REFERENCES AND NOTES

1. S. Wang, S. P. Jiang, Prospects of fuel cell technologies. *Natl. Sci. Rev.* **4**, 163–166 (2017).
2. J. Zhang, Z. Xie, J. Zhang, Y. Tang, C. Song, T. Navessin, Z. Shi, D. Song, H. Wang, D. P. Wilkinson, Z. S. Liu, S. Holdcroft, High temperature PEM fuel cells. *J. Power Sources* **160**, 872–891 (2006).
3. K. V. Kordesch, G. R. Simader, Environmental impact of fuel cell technology. *Chem. Rev.* **95**, 191–207 (1995).
4. D. Aili, D. Henkensmeier, S. Martin, B. Singh, Y. Hu, J. O. Jensen, L. N. Cleemann, Q. Li, Polybenzimidazole-based high-temperature polymer electrolyte membrane fuel cells: New insights and recent progress. *Electrochem. Energy R* **3**, 793–845 (2020).
5. Y. Liu, W. Lehnert, H. Janßen, R. C. Samsun, D. Stolten, A review of high-temperature polymer electrolyte membrane fuel-cell (HT-PEMFC)-based auxiliary power units for diesel-powered road vehicles. *J. Power Sources* **311**, 91–102 (2016).
6. Y. Budak, Y. Devrim, Investigation of micro-combined heat and power application of PEM fuel cell systems. *Energ. Conver. Manage.* **160**, 486–494 (2018).
7. G. Jeong, M. J. Kim, J. Han, H. J. Kim, Y. G. Shul, E. A. Cho, High-performance membrane-electrode assembly with an optimal polytetrafluoroethylene content for high-temperature polymer electrolyte membrane fuel cells. *J. Power Sources* **323**, 142–146 (2016).
8. R. Zeis, Materials and characterization techniques for high-temperature polymer electrolyte membrane fuel cells. *Beilstein. J. Nanotechnol.* **6**, 68–83 (2015).
9. J. Zhang, H. Bai, W. Yan, J. Zhang, H. Wang, Y. Xiang, S. Lu, Enhancing cell performance and durability of high temperature polymer electrolyte membrane fuel cells by inhibiting the formation of cracks in catalyst layers. *J. Electrochem. Soc.* **167**, 114501 (2020).
10. Q. He, B. Shyam, M. Nishijima, D. Ramaker, S. Mukerjee, Mitigating phosphate anion poisoning of cathodic Pt/C catalysts in phosphoric acid fuel cells. *J. Phys. Chem. C* **117**, 4877–4887 (2013).
11. K. Klinedinst, J. A. S. Bett, J. Macdonald, P. Stonehart, Oxygen solubility and diffusivity in hot concentrated H_3PO_4. *J. Electroanal. Chem.* **57**, 281–289 (1974).
12. K. Duan, L. Zhu, M. Li, L. Xiao, N. Bevilacqua, L. Eifert, I. Manke, H. Markötter, R. Zhang, R. Zeis, P. C. Sui, Multiphase and pore scale modeling on catalyst layer of high-temperature polymer electrolyte membrane fuel cell. *J. Electrochem. Soc.* **168**, 054521 (2021).
13. K.-S. Lee, J. S. Spendelow, Y.-K. Choe, C. Fujimoto, Y. S. Kim, An operationally flexible fuel cell based on quaternary ammonium-biphosphate ion pairs. *Nat. Energy* **1**, 2058–7546 (2016).
14. A. S. Lee, Y.-K. Choe, I. Matanovic, Y. S. Kim, The energetics of phosphoric acid interactions reveals a new acid loss mechanism. *J. Mater. Chem. A* **7**, 9867–9876 (2019).
15. V. Atanasov, A. S. Lee, E. J. Park, S. Maurya, E. D. Baca, C. Fujimoto, M. Hibbs, I. Matanovic, J. Kerres, Y. S. Kim, Synergistically integrated phosphonated poly(pentafluorostyrene) for fuel cells. *Nat. Mater.* **20**, 370–377 (2021).
16. Ö. Delikaya, N. Bevilacqua, L. Eifert, U. Kunz, R. Zeis, C. Roth, Porous electrospun carbon nanofibers network as an integrated electrode@gas diffusion layer for high temperature polymer electrolyte membrane fuel cells. *Electrochim. Acta* **345**, 136192 (2020).
17. J. Halter, T. Gloor, B. Amoroso, T. J. Schmidt, F. N. Buchi, Wetting properties of porous high temperature polymer electrolyte fuel cells materials with phosphoric acid. *Phys. Chem. Chem. Phys.* **21**, 13126–13134 (2019).
18. J. Halter, N. Bevilacqua, R. Zeis, T. J. Schmidt, F. N. Büchi, The impact of the catalyst layer structure on phosphoric acid migration in HT-PEFC—An operando x-ray tomographic microscopy study. *J. Electroanal. Chem.* **859**, 113832 (2020).
19. J. Halter, F. Marone, T. J. Schmidt, F. N. Buchi, Breaking through the cracks: On the mechanism of phosphoric acid migration in high temperature polymer electrolyte fuel cells. *J. Electrochem. Soc.* **165**, F1176–F1183 (2018).
20. S. Zhang, J. Zhang, Z. Zhu, P. Liu, F. Cao, J. Chen, Q. He, M. Dou, S. Nan, S. Lu, Unusual influence of binder composition and phosphoric acid leaching on oxygen mass transport in catalyst layers of high-temperature proton exchange membrane fuel cells. *J. Power Sources* **473**, 228616 (2020).
21. J. Lobato, P. Cañizares, M. A. Rodrigo, J. J. Linares, F. J. Pinar, Study of the influence of the amount of PBI–H_3PO_4 in the catalytic layer of a high temperature PEMFC. *Int. J. Hydrogen Energy* **35**, 1347–1355 (2010).
22. J. O. Park, K. Kwon, M. D. Cho, S. G. Hong, T. Y. Kim, D. Y. Yoo, Role of binders in high temperature PEMFC electrode. *J. Electrochem. Soc.* **158**, B675–B681 (2011).
23. J.-H. Kim, H.-J. Kim, T.-H. Lim, H.-I. Lee, Dependence of the performance of a high-temperature polymer electrolyte fuel cell on phosphoric acid-doped polybenzimidazole ionomer content in cathode catalyst layer. *J. Power Sources* **170**, 275–280 (2007).
24. S. Liu, K. Wippermann, W. Lehnert, Mechanism of action of polytetrafluoroethylene binder on the performance and durability of high-temperature polymer electrolyte fuel cells. *Int. J. Hydrogen Energy* **46**, 14687–14698 (2021).
25. H. Su, S. Pasupathi, B. Bladergroen, V. Linkov, B. G. Pollet, Optimization of gas diffusion electrode for polybenzimidazole-based high temperature proton exchange membrane fuel cell: Evaluation of polymer binders in catalyst layer. *Int. J. Hydrogen Energy* **38**, 11370–11378 (2013).
26. Z. Y. Qu, F. Wang, P. Liu, Q. L. Yu, H. J. H. Brouwers, Super-hydrophobic magnesium oxychloride cement (MOC): From structural control to self-cleaning property evaluation. *Mater. Struct.* **53**, 30 (2020).
27. Y. Yang, X. Li, X. Zheng, Z. Chen, Q. Zhou, Y. Chen, 3D-printed biomimetic super-hydrophobic structure for microdroplet manipulation and oil/water separation. *Adv. Mater.* **30**, 1704912 (2018).
28. J. Y. Huang, Y. C. Lo, J. J. Niu, A. Kushima, X. Qian, L. Zhong, S. X. Mao, J. Li, Nanowire liquid pumps. *Nat. Nanotechnol.* **8**, 277–281 (2013).
29. B. Xu, X. Chen, Z. Shi, L. Meng, D. Wang, L. Jiang, H. Liu, Electrochemical on-site switching of the directional liquid transport on a conical fiber. *Adv. Mater.* **34**, 2200759 (2022).
30. M. Qi, Y. Zeng, M. Hou, Y. Gou, W. Song, H. Chen, G. Wu, Z. Jia, Y. Gao, H. Zhang, Z. Shao, Free-standing and ionomer-free 3D platinum nanotrough fiber network electrode for proton exchange membrane fuel cells. *Appl. Catal. Environ.* **298**, 120504 (2021).
31. R. Sun, Z. Xia, Z. Zhang, X. Xu, F. Jing, S. Wang, G. Sun, Supportless Pt-ionomer hybrid porous nanofibrous networks with self-regulated water management for polymer electrolyte fuel cells. *Mater. Today Nano* **18**, 100215 (2022).
32. W. Qing, X. Shi, Y. Deng, W. Zhang, J. Wang, C. Y. Tang, Robust superhydrophobic-superoleophilic polytetrafluoroethylene nanofibrous membrane for oil/water separation. *J. Membr. Sci.* **540**, 354–361 (2017).
33. P. Thomas, J.-P. Guerbois, G. Russell, B. Briscoe, FTIR study of the thermal degradation of poly (vinyl alcohol). *J. Therm. Anal. Calorim.* **64**, 501–508 (2001).
34. Z. Zhang, Z. Xia, J. Huang, F. Jing, S. Wang, G. Sun, Water-induced electrode poisoning and the mitigation strategy for high temperature polymer electrolyte membrane fuel cells. *J. Energy Chem.* **69**, 569–575 (2022).
35. C. Korte, F. Conti, J. Wackerl, W. Lehnert, *High Temperature Polymer Electrolyte Membrane Fuel Cells: Approaches, Status, and Perspectives*, Q. Li, D. Aili, H. A. Hjuler, J. O. Jensen, Eds. (Springer International Publishing, 2016), pp. 169–194.
36. M. Qi, M. Hou, Y. Zeng, Y. Gao, Y. Yang, L. He, H. Chen, H. Zhang, W. Song, Z. Shao, A robust esterified nanofibre electrode for proton exchange membrane fuel cells. *J. Mater. Chem. A* **8**, 5298–5307 (2020).
37. A. B. D. Cassie, S. Baxter, Wettability of porous surfaces. *Trans. Faraday Society* **40**, 546–551 (1944).
38. N. Nonoyama, S. Okazaki, A. Z. Weber, Y. Ikogi, T. Yoshida, Analysis of oxygen-transport diffusion resistance in proton-exchange-membrane fuel cells. *J. Electrochem. Soc.* **158**, B416 (2011).
39. C. Simon, F. Hasche, H. A. Gasteiger, Influence of the gas diffusion layer compression on the oxygen transport in PEM fuel cells at high water saturation levels. *J. Electrochem. Soc.* **164**, F591–F599 (2017).
40. S. Chan, J. Jankovic, D. Susac, M. S. Saha, M. Tam, H. Yang, F. Ko, Electrospun carbon nanofiber catalyst layers for polymer electrolyte membrane fuel cells: Fabrication and optimization. *J. Mater. Sci.* **53**, 11633–11647 (2018).
41. W. Xiao, Z. Xia, H. Li, R. Sun, S. Wang, G. Sun, Electrochemical interface optimization toward low oxygen transport resistance in high-temperature polymer electrolyte fuel cells. *Energ. Technol.* **8**, 2000085 (2020).
42. Z. Wang, L. Yang, S. Wang, H. Sun, G. Sun, Measurement and separation of cathodic mass transport resistance in high temperature proton exchange membrane fuel cell. *Prog. Nat. Sci. Mater.* **30**, 868–875 (2020).
43. F. Hegge, J. Sharman, R. Moroni, S. Thiele, R. Zengerle, M. Breitwieser, S. Vierrath, Impact of carbon support corrosion on performance losses in polymer electrolyte membrane fuel cells. *J. Electrochem. Soc.* **166**, F956–F962 (2019).
44. E. N. Fuller, P. D. Schettler, J. C. Giddings, New method for prediction of binary gas-phase diffusion coefficients. *Ind. Eng. Chem.* **58**, 18–27 (1966).
45. T. V. Reshetenko, J. St-Pierre, Separation method for oxygen mass transport coefficient in gas and ionomer phases in PEMFC GDE. *J. Electrochem. Soc.* **161**, F1089–F1100 (2014).
46. S. Guan, F. Zhou, J. Tan, M. Pan, Influence of pore size optimization in catalyst layer on the mechanism of oxygen transport resistance in PEMFCs. *Prog. Nat. Sci. Mater. Int.* **30**, 839–845 (2020).

47. R. Sun, Z. Xia, X. Xu, R. Deng, S. Wang, G. Sun, Periodic evolution of the ionomer/catalyst interfacial structures towards proton conductance and oxygen transport in polymer electrolyte membrane fuel cells. *Nano Energy* **75**, 104919 (2020).
48. N. Pimperl, N. Bevilacqua, M. A. Schmid, P. A. Loichet Torres, H. A. el-Sayed, R. Zeis, K. P. Zeyer, Nitrogen-functionalized carbon-supported Pt catalysts implemented in high-temperature polymer electrolyte membrane fuel cell. *J. Power Sources* **507**, 229971 (2021).
49. J. Zhang, H. Wang, W. Li, J. Zhang, D. Lu, W. Yan, Y. Xiang, S. Lu, Effect of catalyst layer microstructures on performance and stability for high temperature polymer electrolyte membrane fuel cells. *J. Power Sources* **505**, 230059 (2021).
50. D.-H. Kim, H.-S. Jung, H. Chun, C. Pak, Enhanced membrane electrode assembly performance by adding PTFE/carbon black for high temperature polymer electrolyte membrane fuel cell. *Int. J. Hydrogen Energy* **46**, 29424–29431 (2021).
51. W. Zhang, D. Yao, L. Tian, Z. Xie, Q. Ma, Q. Xu, S. Pasupathi, L. Xing, H. Su, Enhanced performance of high temperature polymer electrolyte membrane fuel cell using a novel dual catalyst layer structured cathode. *J. Taiwan Inst. Chem. Eng.* **125**, 285–290 (2021).
52. D.-H. Kim, C.-M. Min, E. Lee, J.-S. Lee, C. Pak, Effect of vinylphosphonic acid and polymer binders with phosphate groups on performance of high-temperature polymer electrolyte membrane fuel cell. *Catal. Today* **358**, 333–337 (2020).
53. E. Lee, D.-H. Kim, C. Pak, Effects of cathode catalyst layer fabrication parameters on the performance of high-temperature polymer electrolyte membrane fuel cells. *Appl. Surf. Sci.* **510**, 145461 (2020).
54. S. Martin, P. L. Garcia-Ybarra, J. L. Castillo, Ten-fold reduction from the state-of-the-art platinum loading of electrodes prepared by electrospraying for high temperature proton exchange membrane fuel cells. *Electrochem. Commun.* **93**, 57–61 (2018).
55. D. Yao, W. Zhang, Q. Ma, Q. Xu, S. Pasupathi, H. Su, Achieving high Pt utilization and superior performance of high temperature polymer electrolyte membrane fuel cell by employing low-Pt-content catalyst and microporous layer free electrode design. *J. Power Sources* **426**, 124–133 (2019).
56. H. Su, Q. Xu, J. Chong, H. Li, C. Sita, S. Pasupathi, Eliminating micro-porous layer from gas diffusion electrode for use in high temperature polymer electrolyte membrane fuel cell. *J. Power Sources* **341**, 302–308 (2017).
57. Y. Devrim, E. D. Arica, Investigation of the effect of graphitized carbon nanotube catalyst support for high temperature PEM fuel cells. *Int. J. Hydrogen Energy* **45**, 3609–3617 (2020).
58. S. Martin, J. O. Jensen, Q. Li, P. L. Garcia-Ybarra, J. L. Castillo, Feasibility of ultra-low Pt loading electrodes for high temperature proton exchange membrane fuel cells based in phosphoric acid-doped membrane. *Int. J. Hydrogen Energy* **44**, 28273–28282 (2019).
59. S. Kim, T. D. Myles, H. R. Kunz, D. Kwak, Y. Wang, R. Maric, The effect of binder content on the performance of a high temperature polymer electrolyte membrane fuel cell produced with reactive spray deposition technology. *Electrochim. Acta* **177**, 190–200 (2015).
60. H. Su, T. C. Jao, S. Pasupathi, B. J. Bladergroen, V. Linkov, B. G. Pollet, A novel dual catalyst layer structured gas diffusion electrode for enhanced performance of high temperature proton exchange membrane fuel cell. *J. Power Sources* **246**, 63–67 (2014).
61. H. Su, T.-C. Jao, O. Barron, B. G. Pollet, S. Pasupathi, Low platinum loading for high temperature proton exchange membrane fuel cell developed by ultrasonic spray coating technique. *J. Power Sources* **267**, 155–159 (2014).
62. H. Wang, R. Lin, X. Cai, S. Liu, D. Zhong, Z. Hao, Transition metal dissolution control in Pt-alloy catalyst layers for low Pt-loaded PEMFCs for improving mass transfer. *Int. J. Heat Mass Transfer* **178**, 121615 (2021).
63. M. Ko, E. Padgett, V. Yarlagadda, A. Kongkanand, D. A. Muller, Revealing the nanostructure of mesoporous fuel cell catalyst supports for durable, high-power performance. *J. Electrochem. Soc.* **168**, 024512 (2021).
64. J. Liang, Y. Li, R. Wang, J. Jiang, Cross-dimensional model of the oxygen transport behavior in low-Pt proton exchange membrane fuel cells. *Chem. Eng. J.* **400**, 125796 (2020).
65. G. Doo, S. Yuk, J. H. Lee, S. Choi, D. H. Lee, D. W. Lee, J. Hyun, S. H. Kwon, S. G. Lee, H. T. Kim, Nano-scale control of the ionomer distribution by molecular masking of the Pt surface in PEMFCs. *J. Mater. Chem. A* **8**, 13004–13013 (2020).
66. C. Wang, X. Cheng, X. Yan, S. Shen, C. Ke, G. Wei, J. Zhang, Respective influence of ionomer content on local and bulk oxygen transport resistance in the catalyst layer of PEMFCs with low Pt loading. *J. Electrochem. Soc.* **166**, F239–F245 (2019).
67. X. Cheng, C. Wang, G. Wei, X. Yan, S. Shen, C. Ke, F. Zhu, J. Zhang, Insight into the effect of pore-forming on oxygen transport behavior in ultra-low Pt PEMFCs. *J. Electrochem. Soc.* **166**, F1055–F1061 (2019).
68. C. Wang, X. Cheng, J. Lu, S. Shen, X. Yan, J. Yin, G. Wei, J. Zhang, The experimental measurement of local and bulk oxygen transport resistances in the catalyst layer of proton exchange membrane fuel cells. *J. Phys. Chem. Lett.* **8**, 5848–5852 (2017).
69. A. T. S. Freiberg, M. C. Tucker, A. Z. Weber, Polarization loss correction derived from hydrogen local-resistance measurement in low Pt-loaded polymer-electrolyte fuel cells. *Electrochem. Commun.* **79**, 14–17 (2017).
70. S. Shukla, D. Stanier, M. S. Saha, J. Stumper, M. Secanell, Analysis of inkjet printed PEFC electrodes with varying platinum loading. *J. Electrochem. Soc.* **163**, F677–F687 (2016).
71. J. P. Owejan, J. E. Owejan, W. Gu, Impact of platinum loading and catalyst layer structure on PEMFC performance. *J. Electrochem. Soc.* **160**, F824–F833 (2013).
72. T. A. Greszler, D. Caulk, P. Sinha, The impact of platinum loading on oxygen transport resistance. *J. Electrochem. Soc.* **159**, F831–F840 (2012).
73. Y. Ono, A. Ohma, K. Shinohara, K. Fushinobu, Influence of equivalent weight of ionomer on local oxygen transport resistance in cathode catalyst layers. *J. Electrochem. Soc.* **160**, F779–F787 (2013).
74. A. Kongkanand, V. Yarlagadda, T. R. Garrick, T. E. Moylan, W. Gu, (Plenary) Electrochemical diagnostics and modeling in developing the PEMFC cathode. *ECS Trans.* **75**, 25–34 (2016).

Acknowledgments

Funding: The work was financially supported by the National Key Research and Development Program of China (2021YFB4001200), the National Nature Science Foundation of China (22179130), the Foundation of the Key Laboratory of Chinese Academy of Sciences (CXJJ-21S024), and the Dalian Institute of Chemical Physics (DICP-I202023). **Author contributions:** Z.Z. designed and performed the experiments, analyzed the data, and wrote the manuscript. Z.X. designed the experiments, performed the calculation and CFD simulations, interpreted the data, and wrote and revised the manuscript. J.H. performed the CFD simulations and discussed the calculation results. F.J. pretreated the experimental materials. X.Z. discussed the calculation results and revised the manuscript. H.L. discussed the experimental results and revised the manuscript. S.W. and G.S. supervised the study, designed and interpreted the experiment, and revised the manuscript. All authors participated in data analysis and manuscript discussion. **Competing interests:** The authors declare they have no competing interests. **Data and materials availability:** All data needed to evaluate the conclusions in the paper are present in the paper and/or the Supplementary Materials. All supplementary data have been uploaded to https://doi.org/10.5281/zenodo.7308479.

Submitted 26 July 2022
Accepted 29 December 2022
Published 25 January 2023
10.1126/sciadv.ade1194